Capacitor-voltage feedforward with full delay compensation to improve weak grids adaptability of LCL-filtered grid-connected converters for distributed generation systems

Li, Xiaoqiang; Fang, Jingyang; Tang, Yi; Wu, Xiaojie; Geng, Yiwen

Capacitor Voltage Feedforward with Full Delay Compensation to Improve Weak Grids Adaptability of *LCL*-filtered Grid-connected Converters for Distributed Generation Systems

Xiaoqiang Li, *Member IEEE*, Jingyang Fang, *Student Member IEEE*, Yi Tang, *Member IEEE*, Xiaojie Wu, *Member IEEE*, and Yiwen Geng

Abstract—*LCL*-filtered grid-connected converters are widely used for distributed generation systems. However, the current regulation of such converters is susceptible to weak grid conditions, e.g., grid impedance variation and background harmonics. Paralleling multiple harmonic compensators (HCs) is a commonly used method to suppress the current distortion caused by grid background harmonics, but the control bandwidth should be wide enough to ensure system stability. In order to enhance the adaptability of *LCL*-filtered grid-connected converters under weak grid operation, this paper proposes an improved capacitor voltage feedforward control with full delay compensation. When used with converter-side current feedback, the proposed control can keep system low-frequency characteristic independent of grid impedance and provide a high harmonic rejection capability without using additional HCs. Moreover, it completely avoids the design constraints of *LCL*-filter, i.e. $\omega_r<\omega_s/6$ is required for single-loop converter-side current control. Therefore, a higher resonant frequency can be designed to achieve a wider control bandwidth and to lower the current distortion caused by the paralleled filter capacitor branch. Experimental results are finally presented to verify the proposed control which are also in good agreement with theoretical analysis.

Index Terms—Capacitor voltage feedforward, control bandwidth, delay compensation, grid background harmonics, grid impedance, *LCL*-filter, weak grids.

I. INTRODUCTION

LCL-filtered grid-connected converters have been widely used in power conversion applications, such as distributed generation (DG) systems based on photovoltaic (PV), wind turbine, and energy storage etc. [1], [2]. However, due to their direct interconnection with power grids, *LCL*-filtered grid-connected converters are particularly sensitive to non-ideal grid conditions, e.g., grid impedance [2], background harmonics [1]-[3], and grid voltage sags or swells, which often occur in weak grids [4].

Compared with *L*-filter, *LCL*-filter features high harmonic attenuation at switching frequencies, but it brings a stability challenge to the control system due to the well-known *LCL* resonance, and additional damping methods are required to ensure system stability. Because of the extra power loss of physical resistor-based passive damping, active damping methods based on additional state-variable feedback, e.g., capacitor current and capacitor voltage [5]-[7], have attracted more research interests. However, one or three more sensors are required for implementing the active damping in single-phase or three-phase systems, which may lead to higher costs and failure rate. Yi Tang *et al.* [8] first explored the inherent damping characteristic of converter-side current feedback control, which results in a more stable closed-loop system than grid-side current feedback. However, it has overlooked the impact of control delay on the damping performance. Xiongfei Wang *et al.* [9]-[11] investigated the active damping with only grid-side current through a negative high-pass filter, which is equivalent to paralleling a virtual impedance with grid-side inductor. Recently, the effectiveness of conventional notch filter-based active damping has been re-investigated with consideration of control delay and variations of filter parameters and grid impedance, and a design guideline of digital notch filters for robust active damping was developed in [12]. In addition, the stable design regions of *LCL*-filter with single-current-loop control are also revealed in [13], i.e., $\omega_r<\omega_s/6$ for converter-side current feedback, and $\omega_r>\omega_s/6$ for grid-side current feedback, where ω_r and ω_s are the resonant frequency and sampling frequency respectively.

Generally, in order to prevent the large inrush current during startup [14], improve the dynamic response during grid voltage sags or swells [15], and suppress the current distortion caused by grid background harmonics [16], [17], grid voltage at the point of common coupling (PCC) or capacitor voltage is usually measured and fed forward to the control system for disturbances cancellation. However, due to the control delay and high-order *LCL* plants, simple unit voltage feedforward control cannot completely neutralize the impact of grid disturbances on output current regulation, especially those caused by background harmonics. Xuehua

X. Li, J. Fang and Y. Tang are with the School of Electrical and Electronic Engineering, Nanyang Technological University, 639798 Singapore, Singapore (e-mail: lixiaoqiang@ntu.edu.sg; jfang006@e.ntu.edu.sg; yitang@ntu.edu.sg).

X. Wu and Y. Geng are with the School of Information and Electrical Engineering, China University of Mining and Technology, Xuzhou 221116, China. (e-mail: zgcumt@126.com; gengyw556@126.com).

Wang *et al.* [18] thus proposed a full feedforward scheme of grid voltage, which involves a derivative and even a second-order derivative in the feedforward function. It is particularly difficult to implement a precise high-order derivative in the digital control system due to the noise amplification. Paralleling multiple harmonic compensators (HCs) with fundamental proportional-integral (PI) or proportional-resonant (PR) current controller is a commonly used method to attenuate current harmonics [3], [19], [20], but the control bandwidth should be wide enough to cover all the resonant frequencies of HCs [2], [21]. However, the increasing use of distributed generation, low-voltage distribution transformers, and long distribution cables, etc. may cause grid impedance to vary in a wide range, thus leading to a significantly decreased control bandwidth [2]. Instead of compensating harmonics, HCs will then excite low-frequency instability when the control bandwidth is lower than the resonant frequencies of HCs [2]. In addition, the decreased resonant frequency of *LCL*-filter due to inductive grid impedance may cause *LCL*-filter resonance even through the active damping method is employed [5], [6]. Moreover, an additional positive feedback of grid-side current by grid impedance is embedded implicitly in the feedforward path of PCC voltage, which yields a minor current loop. This minor loop changes the low-frequency characteristic of the system, and the stability margin is decreased significantly [22].

Typically, two sets of sensors, one set of current sensors for current feedback control and another set of voltage sensors for grid synchronization, are the basic requirements for proper control of grid-connected converters. Fig. 1 shows the topology of an *LCL*-filter and possible sensed control variables. The control variables can be classified into four groups, i.e., $i_1 \& v_{pcc}$, $i_1 \& v_c$, $i_2 \& v_{pcc}$, and $i_2 \& v_c$. In practical industrial applications, converter-side current i_1 is usually sensed for current feedback control and overcurrent protection in spite of its poor output power quality, i.e., reactive power and harmonics. Since capacitor voltage v_c is linear with PCC voltage v_{pcc}, it is commonly used for grid synchronization. In addition, due to its damping features, capacitor voltage v_c can also be used as a state-variable for active damping [7], [23]-[25]. Based on the above considerations, the group, $i_1 \& v_c$, is selected and discussed in this paper due to its low cost, fast overcurrent protection and resonance damping [24], [25]. This group of control variables is also a promising choice for dual-mode applications, i.e., grid-connected mode and stand-alone mode, in DG and micro-grid systems based on renewable energy.

Active damping techniques based on capacitor voltage have been well investigated in literature. One commonly used method is the virtual impedance control [26]-[28]. In [26], harmonic components of the capacitor voltage are extracted to generate the inner current reference. However, it needs a high control bandwidth for harmonic current tracking, thus high dynamic current control such as deadbeat
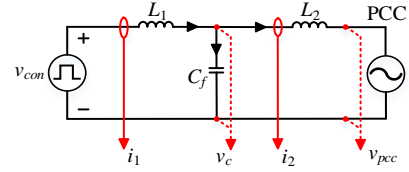

Fig. 1. Topology of an *LCL*-filter and possible sensed control variables.

control, should be employed instead of the conventional PR or PI-based current control. In [27] and [28], an additional state-variable is fed forward with a specific function to form the desirable virtual impedance. However, it demands a noise-sensitive derivative term for the capacitor voltage [29]. In order to avoid the noise amplification at high frequencies, two highly accurate derivatives based on second-order or non-ideal generalized integrator are proposed in [7] recently. Nevertheless, it suffers from damping failure under weak power grids as it is equivalent to that with proportional capacitor-current-feedback [7]. In addition, this derivative-based feedforward form for active damping cannot prevent the large inrush current during startup and suppress the disturbances of grid voltage as mentioned before.

In order to improve the weak grids adaptability of *LCL*-filtered grid-connected converters, this paper proposes a full delay compensation strategy for unit capacitor voltage feedforward, and the digital implementation of the proposed one and a half sampling periods delay compensation does not require derivative operation or additional sensing variables. When incorporated with converter-side current feedback, the proposed method can reshape the low-frequency characteristic of current control and make it independent of grid impedance. Therefore, the control bandwidth keeps unchanged regardless of the variation of grid impedance under week grid conditions. It is also proved that the system has very low output admittance over a wide range of frequencies, and it is possible to achieve good grid background harmonic rejection even with line frequency variation. The multiple HCs used in parallel with the conventional current control can be eliminated, which greatly simplifies the current controller design. Moreover, the resonance frequency of *LCL*-filter can be designed to be above 1/6 of the system sampling frequency, indicating a wider control bandwidth and lower current distortion caused by the paralleled filter capacitor branch. All these findings have not been reported in literature and could be deemed as the main contributions of this paper. Because of the voltage feedforward mechanism, other grid disturbances, e.g. voltage swells or sags, can be also canceled, ensuring fast dynamic response of current control. Experimental results are finally provided to verify the proposed control method.

II. SYSTEM DESCRIPTION AND MODELING

Fig. 2 shows a single-phase *LCL*-filtered grid-connected converter and its basic control structure, where converter-side current i_1 is sensed for closed-loop feedback control and overcurrent protection, and capacitor voltage v_c is
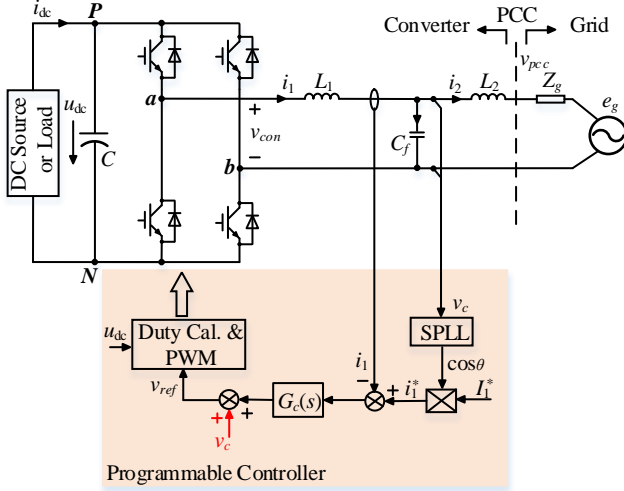
Fig. 2. A single-phase *LCL*-filtered grid-connected converter with converter-side current feedback.

sensed for synchronization, *LCL* resonance damping, and suppression of grid voltage disturbances with its unit feedforward. The *LCL*-filter includes a converter-side inductor L_1, a grid-side inductor L_2, and a filter capacitor C_f. The equivalent grid impedance Z_g can be modeled by the Thevenin's theorem at PCC, and it is purely inductive with L_g here to present the worst case without any physical damping. e_g and v_{pcc} denote grid voltage and PCC voltage respectively. v_{con} denotes output voltage of the converter. u_{dc} and i_{dc} denote dc-side voltage and current respectively. Unipolar sinusoidal pulse-width-modulation (SPWM) and a second-order generalized integrator-based phase-locked loop (SOGI-PLL) are employed to obtain gating and synchronization signals [30], [31].

Fig. 3 shows the mixed-domain current-loop structure that involves the digital current control and continuous *s*-domain plant model. $G_c(s)$ is the current controller consisting of a fundamental PR controller to achieve main power control and multiple HCs to eliminate low-order current harmonics with integral gains k_{i1}, k_{ih} and proportional gain k_p, expressed as

$$G_c(s) = \underbrace{k_p + \frac{k_{i1}\omega_b s}{s^2 + \omega_b s + \omega_1^2}}_{\text{PR}} + \underbrace{\sum_{h=3,5,7\ldots} \frac{k_{ih}\omega_{bh} s}{s^2 + \omega_{bh} s + \omega_h^2}}_{\text{HC}} . \quad (1)$$

T_s is the sampling period. z^{-1} is the computation delay of one sampling period and $G_{zoh}(s)$ is the zero-order-hold (ZOH) given by

$$G_{zoh}(s) = \frac{1 - e^{-T_s s}}{s} . \quad (2)$$

For the sake of analysis, Fig. 4 shows the simplified current control diagrams in the continuous *s*-domain and discrete *z*-domain respectively, where $G_d(s)$ is the equivalent 1.5 sampling periods delay, derived as

$$G_d(s) = \frac{1}{T_s} e^{-T_s s} G_{zoh}(s) \approx e^{-1.5 T_s s} . \quad (3)$$

$G_{i1}(s)$ and $G_{vc}(s)$ are the transfer functions from $v_{con}(s)$ to $i_1(s)$ and $v_c(s)$, respectively. Define $L_T = L_2 + L_g$, it then yields

$$G_{i1}(s) = \frac{1}{L_1 L_T C_f} \cdot \frac{L_T C_f s^2 + 1}{s(s^2 + \omega_r^2)} , \quad (4)$$

$$G_{vc}(s) = \frac{1}{L_1 C_f} \cdot \frac{1}{(s^2 + \omega_r^2)} , \quad (5)$$

where ω_r is the resonant angular frequency,

$$\omega_r = \sqrt{\frac{L_1 + L_T}{L_1 L_T C_f}} . \quad (6)$$

Applying the ZOH *z*-transformation to (4) and (5), it can be derived as

$$G_{i1}(z) = Z[G_{zoh}(s)G_{i1}(s)]$$
$$= \frac{T_s}{(L_1 + L_T)(z - 1)} + \frac{L_T \sin(\omega_r T_s)}{L_1(L_1 + L_T)\omega_r} \cdot \frac{z - 1}{z^2 - 2z\cos(\omega_r T_s) + 1} , \quad (7)$$

$$G_{vc}(z) = Z[G_{zoh}(s)G_{vc}(s)]$$
$$= \frac{L_T(1 - \cos(\omega_r T_s))}{L_1 + L_T} \cdot \frac{z + 1}{z^2 - 2z\cos(\omega_r T_s) + 1} . \quad (8)$$
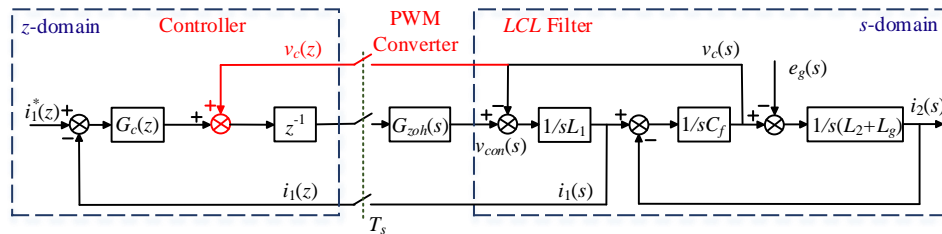

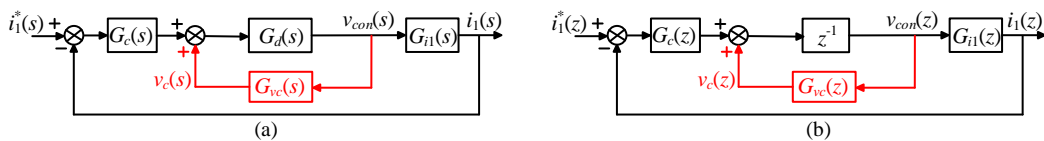Fig. 3. Current-loop control structure in the mixed-domain.

Fig. 4. Simplified current-loop control diagrams. (a) In the continuous *s*-domain. (b) In the discrete *z*-domain.

III. SINGLE-CURRENT-LOOP CONTROL WITHOUT CAPACITOR VOLTAGE FEEDFORWARD

As analyzed in literature, single-current-loop control with converter-side current feedback can be stable only when the resonant frequency ω_r is less than one-sixth of the sampling frequency ω_s, i.e., $\omega_r < \omega_s/6$ [13]. The open-loop transfer function $T_{op1}(z)$ can be derived as (9) from Fig. 4 without considering capacitor voltage feedforward. Fig. 5 shows the bode plots of the open-loop transfer function $T_{op1}(z)$, where $L_g=0$, $C_f=5$ μF and 25 μF respectively, and other parameters are listed in Table I. For the sake of simplicity, only proportional gain k_p is considered with $k_p=1$. As seen, the -180° crossing takes place at $\omega_s/6$ when $\omega_r < \omega_s/6$, while at ω_r and $\omega_s/6$ when $\omega_r > \omega_s/6$ (Here, the -180° crossing at the zero is not considered). According to Nyquist stability criterion, the system is stable only if there are no encirclements of (-1, $j0$) due to no unstable open-loop poles. From Fig. 5, it is obvious that the infinite open-loop gain at ω_r will lead to two encirclements of (-1, $j0$) when $\omega_r > \omega_s/6$, then the system is unstable.

$$T_{op1}(z) = z^{-1}G_c(z)G_{i1}(z) = \frac{G_c(z)}{L_1(L_1+L_T)\omega_r} \cdot$$
$$\frac{L_1\omega_r T_s[z^2 - 2z\cos(\omega_r T_s)+1] + L_T \sin(\omega_r T_s)(z-1)^2}{z(z-1)[z^2 - 2z\cos(\omega_r T_s)+1]} \quad (9)$$

However, it is not sufficient to ensure system stability only with the constraint of $\omega_r < \omega_s/6$. The proportional gain k_p should satisfy the following condition

$$T_{op1}(z = e^{j\frac{\omega_s}{6}T_s}) < 0\,\text{dB}$$
$$\Rightarrow k_p < \frac{L_1(L_1+L_T)\omega_r(1-2\cos(\omega_r T_s))}{L_T \sin(\omega_r T_s) - L_1\omega_r T_s(1-2\cos(\omega_r T_s))} \quad (10)$$

It is known that the limitation of resonant frequency ($\omega_r < \omega_s/6$) will lead to a low control bandwidth, which then results in slow transient response. Moreover, in order to suppress the current distortion arising from low-order grid background harmonics, multiple HCs are usually paralleled with the fundamental PR controller as (1). This requires a wide enough control bandwidth to cover all the resonant frequencies of HCs, or the system may be unstable. The low control bandwidth will limit the number of harmonics to be compensated by HCs. In addition, the above situations may get worse when large inductive grid impedance L_g appears which decreases the control bandwidth. Fig. 6 shows the bode plots of the open-loop transfer function $T_{op1}(z)$ with 5th and 7th HCs, where $k_p=4$ and $C_f=25$ μF with resonant frequency being 1.46 kHz ($< f_s/6$). f_c is the cut-off frequency. As seen from Fig. 6(b), with the requirements of $\omega_r < \omega_s/6$ and (10), f_{c1} is close to the 7th harmonic frequency, thus the highest harmonic to be compensated is 7th. Near the 7th harmonic frequency, there is one negative and one positive -180° crossing at f_1 and f_2 respectively. Since the magnitude of $T_{op1}(z)$ is always greater than 0dB at these two frequencies, the total number of encirclements of (-1, $j0$) is
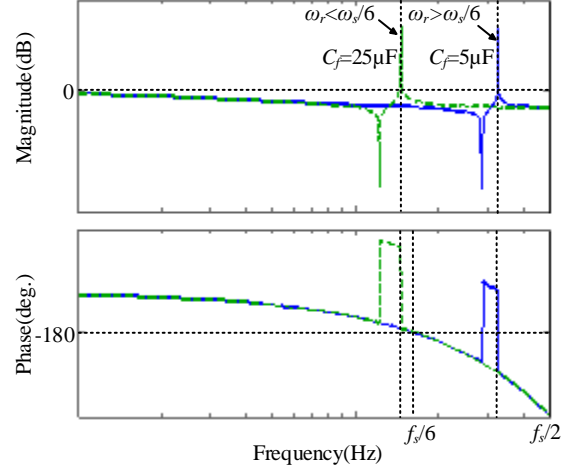

Fig. 5. Bode plots of the open-loop transfer function $T_{op1}(z)$ with $\omega_r < \omega_s/6$ and $\omega_r > \omega_s/6$.

TABLE I
PARAMETERS OF *LCL*-FILTER

Description	Symbol	Value
Filter capacitance	C_f/μF	3~25
Converter-side inductance	L_1/mH	1.5
Grid-side inductance	L_2/mH	0.7
Grid impedance	L_g/mH	0 / 2
Sampling frequency	f_s/kHz	10

zero, and the system is stable. However, with the increase of L_g, the cut-off frequency f_{c1} decreases to f_{c2}, and the magnitude of $T_{op1}(z)$ at f_2 is less than 0dB. Hence, there will be two encirclements of (-1, $j0$) (considering the negative frequency), and it causes the system to be unstable.

Since the grid-side current feedback control is the direct regulation of output current, the current distortion can be well suppressed by HCs. While for the converter-side current feedback control, the output current inevitably contains certain harmonics due to the paralleled filter capacitor branch. However, to satisfy the stability requirement, $\omega_r < \omega_s/6$, a large capacitance is usually employed to obtain a lower resonant frequency. Large capacitance will then aggravate the output current distortion. In order to explain this, Fig. 7 shows the grid-side current diagram with converter-side current feedback control, where grid voltage $e_g(s)$ as a harmonic source needs to be considered. The transfer function $G_{i2}(s)$, $G_{gi2}(s)$ and $G_{gi1}(s)$ are given as follows

$$\begin{cases} G_{i2}(s) = \dfrac{1}{L_1 L_T C_f} \cdot \dfrac{1}{s(s^2+\omega_r^2)} \\[3mm] G_{gi2}(s) = \dfrac{1}{L_1 L_T C_f} \cdot \dfrac{L_1 C_f s^2 + 1}{s(s^2+\omega_r^2)} \\[3mm] G_{gi1}(s) = \dfrac{1}{L_1 L_T C_f} \cdot \dfrac{1}{s(s^2+\omega_r^2)} \end{cases} \quad (11)$$
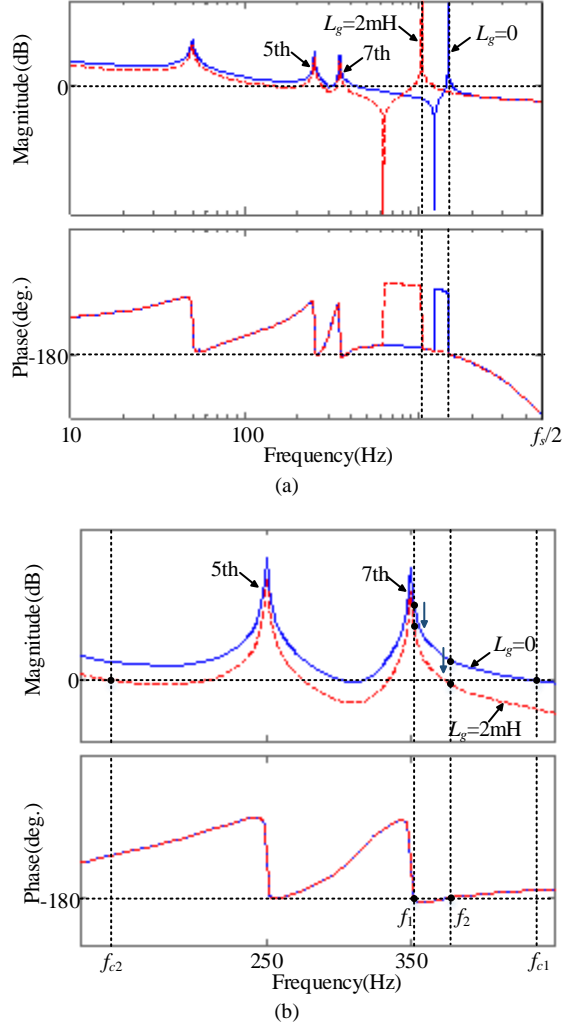
Fig. 6. Bode plots of the open-loop transfer function $T_{op1}(z)$ with 5th and 7th HCs. (a) Full view. (b) Zoomed-in view in 5th and 7th harmonic frequencies.

Then, the output admittance $Y_{o1}(s)$ can be derived as (12) from Fig. 7.

$$Y_{o1}(s) = -\frac{i_2(s)}{e_g(s)} = G_{gi2}(s) - \frac{G_d(s)G_c(s)G_{i2}(s)G_{gi1}(s)}{1 + G_d(s)G_c(s)G_{i1}(s)} \quad (12)$$

Fig. 8 shows the magnitude-frequency curves of the output admittance $Y_{o1}(s)$ with three different filter capacitances C_f=5 μF, 10 μF and 25 μF, where L_g=0 and k_p=4. As seen, with the increase of C_f, the magnitude of the output admittance $Y_{o1}(s)$ at the compensated harmonic frequencies by HCs increases, which indicates that the capability of suppressing grid background harmonics decreases.

From the above analysis, it can be known that the single-current-loop control with converter-side current feedback has a poor adaptability under weak grids, which is due to its limited design region of *LCL*-filter and also its sensitivity to grid impedance variation.
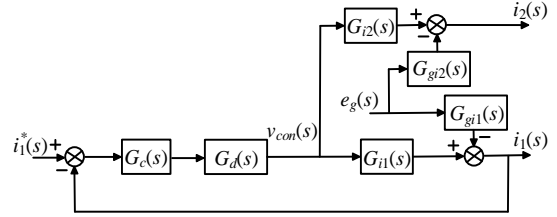

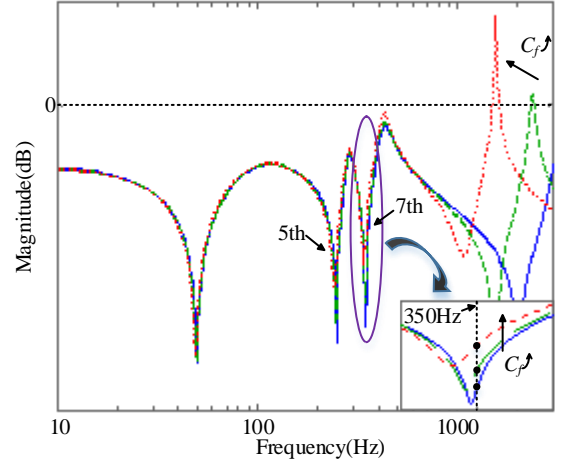Fig. 7. Grid-side current diagram with converter-side current feedback control.

Fig. 8. Magnitude-frequency curves of the output admittance $Y_{o1}(s)$ with different filter capacitance C_f.

IV. CONVERTER-SIDE CURRENT CONTROL WITH UNIT CAPACITOR VOLTAGE FEEDFORWARD

Generally, in order to prevent the large inrush current during startup and suppress the disturbances of grid voltage, unit PCC voltage or capacitor voltage can be used as a feedforward term to decouple the actual grid voltage. In this paper, considering the resonance damping, unit capacitor voltage feedforward is employed as discussed in Introduction, shown in Fig. 2.

From Fig. 4(b), the open-loop transfer function $T_{op2}(z)$ is derived as follows

$$T_{op2}(z) = G_c(z)G_{in}(z)G_{i1}(z) = \frac{z^{-1}G_c(z)G_{i1}(z)}{1 - z^{-1}G_{vc}(z)}, \quad (13)$$

where $G_{in}(z)$ is the minor loop.

According to Nyquist stability criterion, the pole locations of $T_{op2}(z)$ need to be investigated. From (13), the unstable poles of $T_{op2}(z)$ can be identified by applying Nyquist stability criterion to $T_{in}(z)=-z^{-1}G_{vc}(z)$. Since $G_{vc}(z)$ has no unstable poles, the unstable poles of $T_{op2}(z)$ are then determined by the encirclements of (-1, j0) by $T_{in}(z)$. Fig. 9 shows the bode plots of the minor loop gain $T_{in}(z)$, where L_g=0, L_1, L_2 and f_s are listed in Table I, and C_f is purposely set as 3μF, 5.5 μF and 15 μF for analysis with resonant frequency 4.21 kHz, 3.12 kHz and 1.88 kHz respectively. As seen, the -180° crossing takes place at $\omega_s/3$ when $\omega_r<\omega_s/3$, while at ω_r when $\omega_r>\omega_s/3$. In order to explain this situation, the value of $T_{in}(z)$ at $\omega_s/3$ can be calculated as
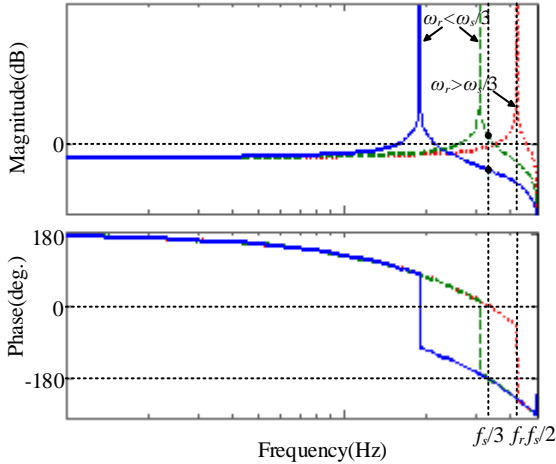
Fig. 9. Bode plots of the minor loop gain $T_{in}(z)$.

Fig. 10. Curves of two functions in (15) with the increase of L_g.

$$T_{in}(z = e^{j\frac{\omega_s}{3}T_s}) = -\frac{L_T(1-\cos(\omega_r T_s))}{(L_1+L_T)(1+2\cos(\omega_r T_s))}. \qquad (14)$$

From (14), it can be seen $T_{in}(z)$ at $\omega_s/3$ is negative when $\omega_r < \omega_s/3$ and positive when $\omega_r > \omega_s/3$. Thus, -180° crossing always takes place at $\omega_s/3$ when $\omega_r < \omega_s/3$. In order to avoid the encirclements of (-1, j0), the resonant frequency ω_r should be less than $\omega_s/3$. However, it is not sufficient to ensure that $T_{op2}(z)$ has no unstable poles. As the dashed bode plot shown in Fig. 9, there are two encirclements of (-1, j0) due to the magnitude of $T_{in}(z)$ at $\omega_s/3$ being greater than 0 dB even though $\omega_r < \omega_s/3$. Hence, in addition to the design of resonant frequency ω_r, the magnitude of $T_{in}(z)$ at $\omega_s/3$ should be less than 0 dB. Based on (14), it can be derived as follows

$$20\lg\left|T_{in}(z = e^{j\frac{\omega_s}{3}T_s})\right| < 0\text{dB} \Rightarrow \cos(\omega_r T_s) > -\frac{L_1}{2L_1+3L_T}. \qquad (15)$$

The constraint conditions, $\omega_r < \omega_s/3$ and (15), are then given to ensure that the open-loop transfer function $T_{op2}(z)$ has no unstable poles. As seen, (15) is always valid when $\omega_r < \omega_s/4$ due to $\cos(\omega_r T_s) > 0$. While for $\omega_s/4 < \omega_r < \omega_s/3$, it is difficult to determine which side of (15) is greater due to the potential grid impedance L_g and its complicated functions, e.g., trigonometric function and square-root operation. It may decrease the upper limit of resonant frequency and make it lower than than $\omega_s/3$. Given that $L_g=0$, and $L_1=1.5$ mH, $L_2=0.7$ mH, and $f_s=10$ kHz listed in Table I, the available range of filter capacitance is found to be $C_f > 6$ μF by (15), and thus the upper limit of ω_r is 2.97 kHz which is less than $\omega_s/3=3.33$ kHz. Taking $C_f=7$μF, Fig. 10 shows the curves of two functions in (15) with the increase of L_g. As seen, the inequality is always valid which indicates that $T_{op2}(z)$ has no open-loop unstable poles with this set of LCL parameters regardless of grid impedance variation.

Following the above design constraints, $T_{op2}(z)$ should have no encirclements of (-1, j0) to ensure system stability by Nyquist stability criterion. With the same L_1, L_2 and f_s as 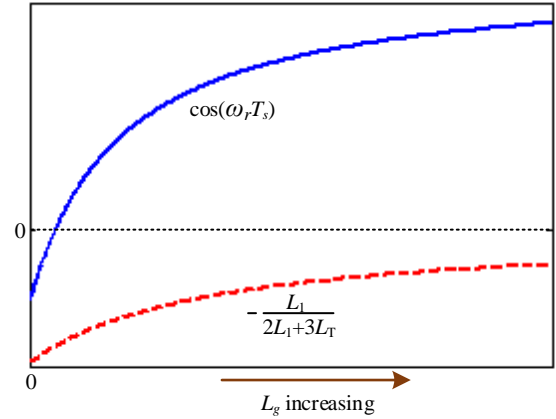above and $k_p=1$, Fig. 11 shows the bode plots of the open-loop transfer function $T_{op2}(z)$, where C_f is set as 7μF and 10μF with resonant frequency being 2.75 kHz and 2.30 kHz respectively. As seen, LCL resonance damping is enhanced with the increase of filter capacitance C_f. It indicates that a large proportional gain k_p can be allowed by employing a large filter capacitance, thus leading to a high control bandwidth. Even though large filter capacitance can result in higher control bandwidth to parallel more HCs, it causes increased current distortion due to paralleled filter capacitor branch.

Further, in order to investigate the robustness against grid impedance variation, Fig. 12 shows the bode plots of $T_{op2}(z)$ with grid impedance L_g, where C_f is 10 μF to damp the resonance peak. As seen, the phase-frequency curve falls off rapidly when $L_g=2$ mH, thus leading to a small phase margin. In addition, the decreased phase margin and decreased magnitude response of $T_{op2}(z)$ will limit its harmonic rejection capability since only a few harmonics can be compensated as analyzed in Fig. 6.

V. PROPOSED CAPACITOR VOLTAGE FEEDFORWARD WITH FULL DELAY COMPENSATION

Section IV has derived the stable design region of LCL-filter when unit capacitor voltage feedforward is employed to suppress grid voltage disturbances, which is obviously wider than single-current-loop control ($\omega_r < \omega_s/6$). However, it still has a poor rejection capability of grid background harmonics and is quite sensitive to grid impedance variation.

From Fig. 4(a), the open-loop transfer function $T_{op2}(s)$ in the continuous s-domain is derived as

$$T_{op2}(s) = \frac{G_c(s)G_d(s)G_{i1}(s)}{1-G_d(s)G_{vc}(s)}$$
$$= \frac{G_c(s)G_d(s)(L_T C_f s^2+1)}{L_1 L_T C_f s^3+(L_1+L_T)s-\underbrace{G_d(s)L_T s}_{\text{Damping Term}}} \qquad (16)$$

From (16), it can be seen a damping term is introduced by unit capacitor voltage feedforward, which contributes to the attenuation of LCL resonance peak shown in Fig. 11 and Fig. 12. Further, the low-frequency characteristic of $T_{op2}(s)$
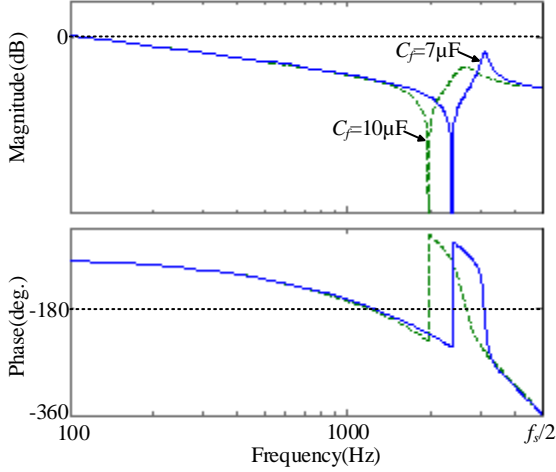
Fig. 11. Bode plots of the open-loop transfer function $T_{op2}(z)$ with different filter capacitance C_f.

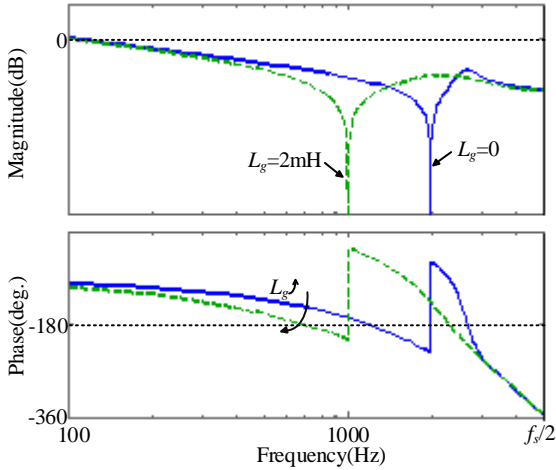
Fig. 12. Bode plots of the open-loop transfer function $T_{op2}(z)$ with grid impedance L_g.

can be approximated by neglecting the high-order terms in (16) as

$$T_{op2}(s) \approx \frac{G_c(s)G_d(s)}{(L_1+L_T)s - G_d(s)L_T s}. \quad (17)$$

As seen from (17), grid impedance L_g (in L_T) changes the magnitude and phase of the denominator. The low-frequency characteristic of $T_{op2}(s)$ is thus affected by L_g as shown in Fig. 12, which leads to a poor grid-adaptability, e.g., reduced stability margin and harmonic rejection capability. If a compensation link $G_{tc}(s)$ is inserted in the feedforward path, as shown in Fig. 13, the open-loop transfer function $T'_{op2}(s)$ then can be derived as

$$T'_{op2}(s) = \frac{G_c(s)G_d(s)(L_T C_f s^2 + 1)}{L_1 L_T C_f s^3 + (L_1 + L_T)s - G_d(s)G_{tc}(s)L_T s}. \quad (18)$$

From (18), if $G_{tc}(s)=1/G_d(s)$, it can be yielded as $T'_{op2}(s)=G_c(s)G_d(s)/L_1 s$. The current control loop becomes a first-order L-filtered system with only converter-side inductance L_1 and independent of grid impedance L_g, which
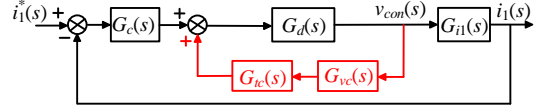

Fig. 13. Current-loop control diagram with compensation link $G_{tc}(s)$.

will lead to a strong adaptability under weak grids. From (3), $G_d(s)$ is the time delay link with one and a half sampling periods. Consequently, $G_{tc}(s)$ should be a time advance link to compensate the delay. Actually, same thought can also be found in [24], where only one sampling period delay is considered to compensate, and its realization takes up too much storage space and is not accurate enough.

A. One Sampling Period Delay Compensation

Several prediction techniques for compensation of one sampling period delay have been proposed earlier, e.g., linear prediction, smith prediction, and repetitive prediction, etc. [32], [33]. However, these techniques are either sensitive to plant parameters or not accurate enough especially in the high-frequency range. [6], [25] and [34] proposed a reduced delay method by shifting the sampling instant of state-variables. However, the sampling number in one sampling period is doubled in [6]. In [25] and [34], the sampling instant needs to be set carefully to implement the control algorithm, and meanwhile, it is difficult to achieve one sampling period delay compensation. More importantly, the sampling-induced aliasing and switching noise may be introduced to the control system. In view of these, an improved reduced delay method is proposed, which shifts the update instant of reference voltage instead of the sampling instant of state-variables.

For comparison, Fig. 14(a) shows the conventional current control structure with unit capacitor voltage feedforward, where $v_{co}(k)$ is the output of current controller, $v_{ref}(k)$ is the reference voltage, and k denotes the k_{th} sampling period. From Fig. 14(a), it can be yielded as

$$v_{ref}(k) = z^{-1}v_r(k) = v_r(k-1) = v_{co}(k-1) + v_c(k-1). \quad (19)$$

From (19), it can be seen the reference voltage v_{ref} at the k_{th} sampling period is the sum of v_{co} and v_c at the $(k-1)_{th}$ sampling period due to one sampling period delay for control algorithm implementation.

Fig. 14(b) shows the sampling and update instants of the digital PWM, where,

Event 1: Sampling instant of converter-side current i_1 and capacitor voltage v_c.

Event 2: Calculation finished instant of v_r which is subsequently used for updating reference voltage v_{ref}.

Event 3: Update instant of reference voltage v_{ref} which is also the sampling instant of next period.

Fig. 15(a) shows the current control structure with the proposed one sampling period delay compensation, and it can be yielded as
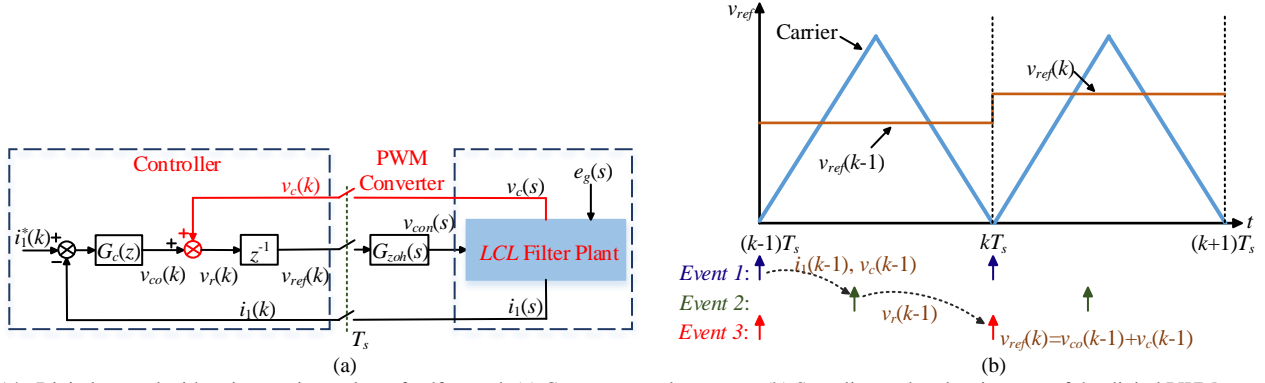
Fig. 14. Digital control with unit capacitor voltage feedforward. (a) Current control structure. (b) Sampling and update instants of the digital PWM.
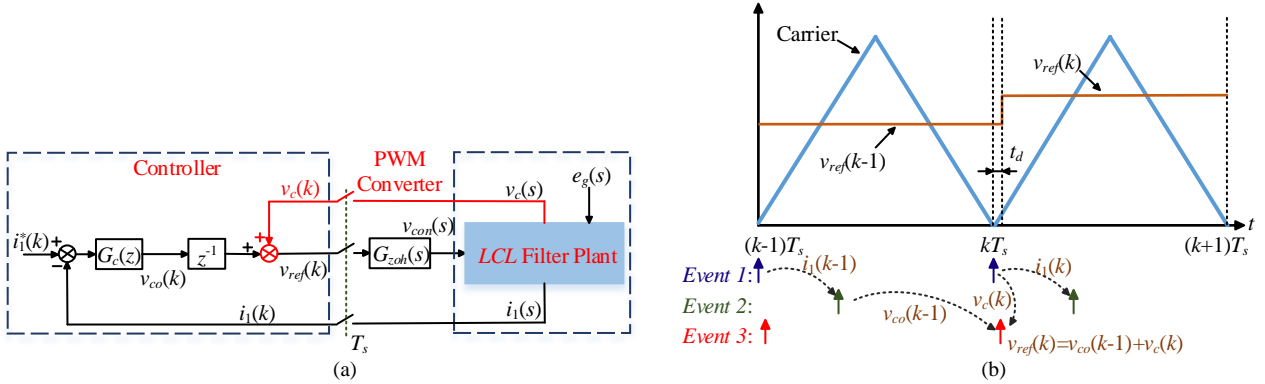

Fig. 15. Digital control with the proposed one sampling period delay compensation. (a) Current control structure. (b) Sampling and update instants of the digital PWM.

$$v_{ref}(k) = z^{-1}v_{co}(k) + v_c(k) = v_{co}(k-1) + v_c(k). \quad (20)$$

In comparison to (19), the reference voltage v_{ref} in (20) at the k_{th} sampling period is the sum of v_{co} at the $(k-1)_{th}$ sampling period and v_c at the k_{th} sampling period. Obviously, the one sampling period delay compensation is realized by changing the feedforward instant of capacitor voltage. With this idea, Fig. 15(b) shows the sampling and update instants which indicates the digital implementation of one sampling period delay compensation, where,

Event 1: Sampling instant of converter-side current i_1 and capacitor voltage v_c.

Event 2: Calculation finished instant of v_{co} which is subsequently used for calculating reference voltage v_{ref}.

Event 3: Update instant of reference voltage v_{ref} with negligible delay t_d to *Event 1*, where t_d consists of the sampling time t_{ad} of analog-to-digital converter (ADC) and the calculation time t_{cd} of half sampling period delay compensation which will be discussed in the following subsection.

As seen from Fig. 15(b), $v_c(k)$ is used for obtaining the reference voltage $v_{ref}(k)$ instead of $v_c(k-1)$ in order to eliminate the one sampling period delay of voltage feedforward. The update instant of reference voltage $v_{ref}(k)$ is slightly shifted by t_d for implementing this delay compensation. It should be noted that the delay time t_d is much smaller as compared to the switching period, and its
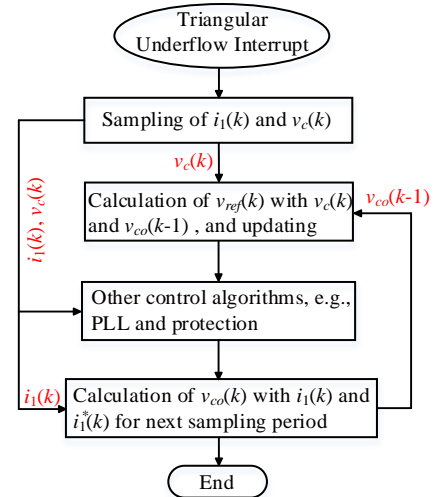
Fig. 16. Digital implementation flowchart of the main control algorithm with one sampling period delay compensation.

impact on the control system could be neglected. If t_d is too large and cannot be ignored due to some slow conversion rate ADCs or very high sampling frequency, some additional control techniques should be employed to improve the control performance of the system, such as the two-polarity PWM method and asymmetric PWM method

proposed in [35], [36]. These modulation methods can tolerate the maximum time of $0.25T_s$ for t_d.

For the sake of easy understanding, Fig. 16 shows the digital implementation flowchart of the main control algorithm with the proposed one sampling period delay compensation.

B. Half Sampling Period Delay Compensation

From (3), the half sampling period delay is caused by the ZOH characteristic of PWM. Unlike one sampling period delay compensation which is realized by changing the feedforward instant of capacitor voltage, an additional compensation link is inserted in the feedforward path to handle the half sampling period delay. Fig. 17 shows the digital current control structure with full delay compensation, where $G_{hc}(z)$ is to compensate the half sampling period delay, expressed as (21). Actually, the similar link can also be found in [5] and [37] to improve the performance of active damping.

$$G_{hc}(z) = \frac{2}{1+z^{-1}} .\qquad (21)$$

Fig. 18 shows the bode plots of $G_{hc}(z)$ and an ideal half sampling period in advance $z^{0.5}$ with sampling frequency f_s=10 kHz. As seen, the phase of $G_{hc}(z)$ has a perfect match with $z^{0.5}$ within Nyquist frequency $f_s/2$. However, its magnitude response increases with the increase of frequency and becomes infinite at $f_s/2$, which is unacceptable because of the sampling noise amplification. In order to explain this, (21) can be expanded as

$$G_{hc}(z = e^{j\omega T_s}) = \frac{2}{1+e^{-j\omega T_s}} = \frac{e^{j0.5\omega T_s}}{\cos(0.5\omega T_s)} .\qquad (22)$$

As seen from (22), the phase of $G_{hc}(z)$ is $0.5\omega T_s$ same as $z^{0.5}$, while the magnitude is $1/\cos(0.5\omega T_s)$ which is infinite at $f_s/2$ due to $\cos(0.5\omega_s T_s/2)=0$. Based on the control structure of repetitive controller, a modified version of (21) is thus proposed shown as Fig. 19, where m is a proportional coefficient with $0<m\leq1$, and $G_{zf}(z)$ is a first-order zero-phase-shift low-pass filter (LPF) having $G_{zf}(z)=d_1z+d_0+d_1z^{-1}$, where $d_0=1-2d_1$ [38], [39]. The modified link is expressed as

$$G'_{hc}(z) = \frac{1+m}{1+mG_{zf}(z)z^{-1}} .\qquad (23)$$

It is noted that there is a 'z' in the $G_{zf}(z)$ which can be hardly realized in the digital control system. Fortunately, another term 'z^{-1}' in the feedback path can be integrated into $G_{zf}(z)$ to cancel 'z'. The value of $G_{zf}(z)$ is calculated as $d_0+2d_1\cos(\omega T_s)$ which features zero phase in the whole frequency range as shown in Fig. 20. By calculation, $G_{zf}(z)$ is equal to d_0-2d_1 at $f_s/2$, and thus, if $d_1=0.25$, $20\lg|G_{zf}(z=e^{j\omega T_s})|\mid_{\omega=\omega_s/2}=-\infty$, as shown in Fig. 20. In order to attenuate the magnitude peak of $G'_{hc}(z)$ effectively, $d_1=0.25$ is selected in this paper, and then the magnitude of $G'_{hc}(z)$ at $f_s/2$ is $1+m$ with the maximum value of 2 due to $0<m\leq1$.
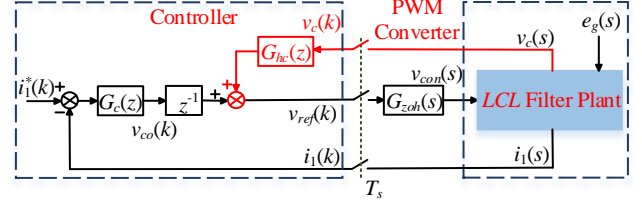

Fig. 17. Digital current control structure with full delay compensation.

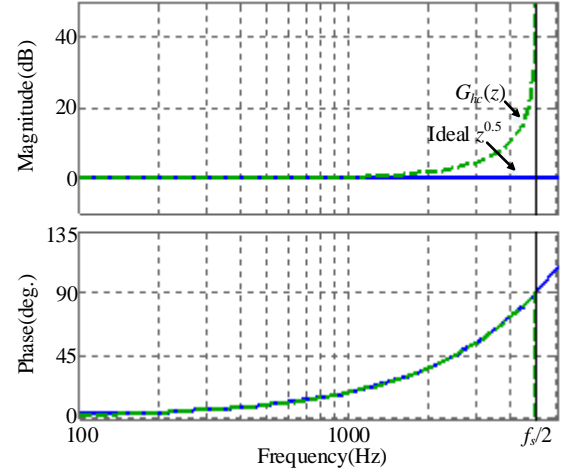

Fig. 18. Bode plots of $G_{hc}(z)$ and ideal $z^{0.5}$.

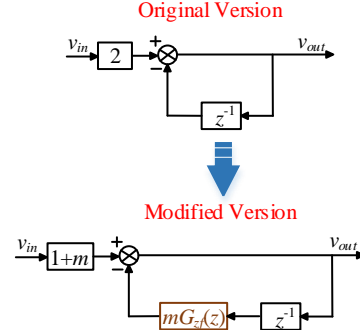
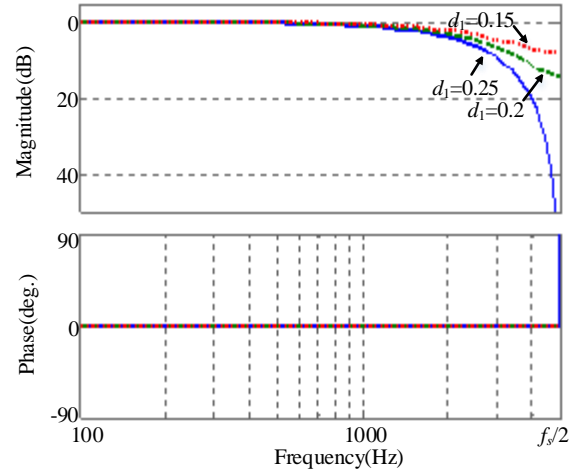Fig. 19. Modified delay compensation link of half sampling period.
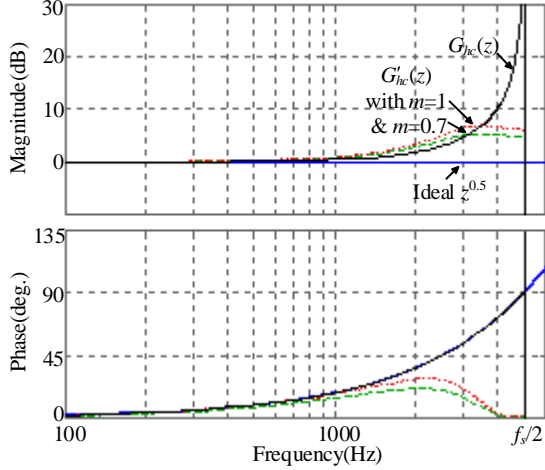

Fig. 20. Bode plots of $G_{zf}(z)$ with different d_1.

Fig. 21. Bode plots of $G_{hc}(z)$, $G'_{hc}(z)$ and ideal $z^{0.5}$.

Fig. 21 shows the bode plots of $G_{hc}(z)$, $G'_{hc}(z)$ and ideal $z^{0.5}$. As seen, the magnitude peak of $G'_{hc}(z)$ is attenuated effectively unlike $G_{hc}(z)$, but the phase in the high-frequency range decreases gradually until zero at $f_s/2$. As discussed in Section IV and the beginning of Section V, grid impedance L_g has a great impact on the low-frequency characteristic of $T_{op2}(z)$, which leads to a poor grid-adaptability. Thus, only the low-frequency range of half sampling period delay needs to be compensated by $G'_{hc}(z)$. From Fig. 21, it can be seen the modified $G'_{hc}(z)$ can simulate ideal $z^{0.5}$ well in the low-frequency range with a proper m. Moreover, it can also be noted that a smaller m gives a better match in magnitude response but poorer phase compensation. In addition to the frequency characteristic of $G'_{hc}(z)$, the stability of current control loop should also be considered for the selection of m, which will be discussed in the following subsection.

C. Stability Analysis and Its Robustness against Grid Impedance

Fig. 22 shows the current-loop control diagram with full delay compensation in the discrete z-domain, and its continuous s-domain form is shown in Fig. 13, where,

$$\begin{cases} G_{tc}(z) = zG'_{hc}(z) \\ G_{tc}(s) = e^{T_s s}G'_{hc}(s) \end{cases}. \qquad (24)$$

From Fig. 22, the open-loop transfer function $T'_{op2}(z)$ is derived as

$$T'_{op2}(z) = G_c(z)G_{inc}(z)G_{i1}(z) = \frac{z^{-1}G_c(z)G_{i1}(z)}{1 - G'_{hc}(z)G_{vc}(z)}. \qquad (25)$$

where $G_{inc}(z)$ is the minor loop.

As analyzed in Section IV, the poles of $T'_{op2}(z)$ are first investigated. From (25), its unstable poles are related to the minor loop $G_{inc}(z)$. Thus, the unstable poles of $T'_{op2}(z)$ can be identified by applying Nyquist stability criterion to $T_{inc}(z)=-G'_{hc}(z)G_{vc}(z)$. As $T_{inc}(z)$ has no unstable poles, only its encirclements of (-1, j0) need to be investigated. Fig. 23 shows the bode plots of $T_{inc}(z)$, where m=0.7, L_g=0 and C_f=5 µF with resonant frequency being 3.26 kHz. For the sake of
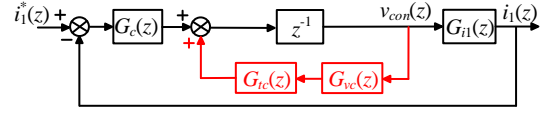

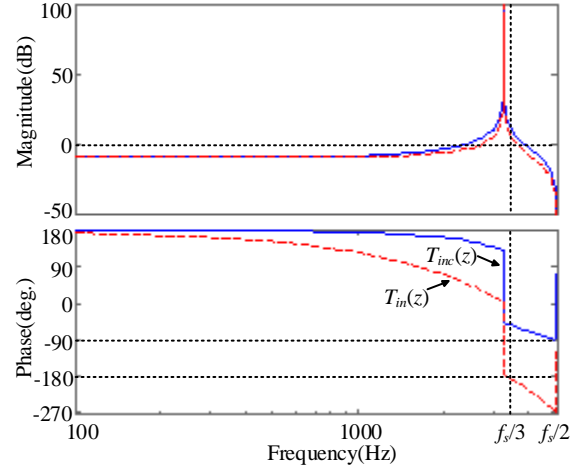Fig. 22. Current-loop control diagram with full delay compensation in the discrete z-domain.

Fig. 23. Bode plots of $T_{inc}(z)$ and $T_{in}(z)$.

comparison, $T_{in}(z)=-z^{-1}G_{vc}(z)$ is also plotted which indicates unit capacitor voltage feedforward without delay compensation. As seen, there is a -180° crossing at $\omega_s/3$ for $T_{in}(z)$, and since the magnitude of $T_{in}(z)$ at $\omega_s/3$ is greater than 0 dB, $T_{op2}(z)$ has two unstable poles. Its detail analysis can be found in Section IV. While for $T_{inc}(z)$, there is always no -180° crossing since the phase lag caused by the delay is compensated by $G_{tc}(z)$. It indicates that $G_{inc}(z)$ or $T'_{op2}(z)$ has no unstable poles, and no additional design constraints for LCL-filter are required unlike $T_{op2}(z)$ with $\omega_r<\omega_s/3$ and (15). Furthermore, a higher resonant frequency can be allowed for converter-side current feedback control, indicating a better rejection capability of grid background harmonics.

Following the analysis of unstable poles of $T'_{op2}(z)$, its encirclements of (-1, j0) are next investigated. Fig. 24 shows the bode plots of $T'_{op2}(z)$ with different m, where the used parameters are the same as above and k_p=1. For comparison, the open-loop transfer function with an L-filter is also plotted, where the inductance L is equal to the converter-side inductance L_1 of LCL-filter. As seen, the low-frequency characteristic of $T'_{op2}(z)$ has a perfect match with the one in L-filter, but the high-frequency does not. It is because 1.5 sampling periods delay $G_d(s)$ is compensated well only in the low-frequency range due to $G'_{hc}(z)$. In Fig. 24, there is only one valid -180° crossing for $T'_{op2}(z)$ as the one in L-filter. According to Nyquist stability criterion, the control system can be stable when a proper proportional gain k_p is selected.

Moreover, it can also be seen that there is a small peak in the magnitude-frequency curves of $T'_{op2}(z)$, near the magnitude trap produced by the zeros of $T'_{op2}(z)$. Ideally, if the delay $G_d(s)$ is compensated completely in the whole

frequency range, the zeros can cancel the resonant poles as discussed in the beginning of Section V. Then, the current control loop is an *L*-filtered first-order system. However, due to the non-ideal high-frequency characteristic of $G'_{hc}(z)$ to compensate the half sampling period delay, the poles mismatch the zeros which leads to a small peak, as shown in Fig. 24. The peak caused by the poles is attenuated gradually with the decrease of *m*. Thus, a larger proportional gain k_p can be allowed by selecting a smaller *m*.

In order to show the superior robustness of the proposed method under grid impedance variation, Fig. 25 shows the bode plots of $T'_{op2}(z)$ and $T_{op2}(z)$, where $m=0.7$ for $T'_{op2}(z)$, $C_f=5$ μF and other parameters are listed in Table I. As seen, with the proposed method, the low-frequency characteristic of $T'_{op2}(z)$ keeps unchanged regardless of grid impedance L_g. Thus, the control system has an invariant phase margin and control bandwidth independent of grid impedance L_g. While for $T_{op2}(z)$ with unit capacitor voltage feedforward, its significant phase variation leads to a small stability margin and even instability.

D. Suppression of Grid Background Harmonics

In addition to grid impedance variation, grid background harmonics may also exist in weak grids. The harmonic rejection capability will be investigated from the output admittance perspective. Fig. 26 shows the grid-side current diagram with converter-side current feedback control and the proposed capacitor voltage feedforward method, where G_{gvc} is the transfer function from e_g to capacitor voltage v_c, expressed as

$$G_{gvc}(s) = \frac{1}{L_T C_f} \cdot \frac{1}{s^2 + \omega_r^2} . \qquad (26)$$

From Fig. 26, it can be derived as

$$Y_{oc}(s) = -\frac{i_2(s)}{e_g(s)}$$

$$= G_{gi2}(s) - \frac{G_d(s)G_{i2}(s)[G_c(s)G_{gi1}(s) + G_{tc}(s)G_{gvc}(s)]}{1 + G_d(s)G_c(s)G_{i1}(s) - G_{tc}(s)G_d(s)G_{vc}(s)} . \qquad (27)$$

Substituting (3)-(5), (11), (26) into (27) yields (28), shown at the bottom of next page.

By neglecting the high-order terms, (28) can be approximated as (29) with $G_{tc}(s) \approx 1/G_d(s)$ in the low-frequency range, also shown at the bottom of next page.

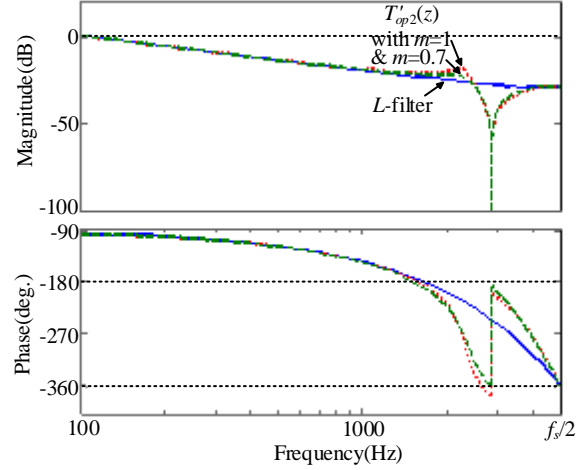Fig. 24. Bode plots of the open-loop transfer function $T'_{op2}(z)$ with different *m*.

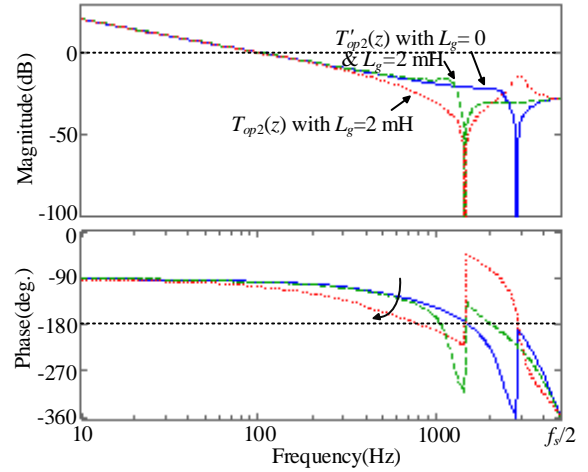
Fig. 25. Bode plots of the open-loop transfer function $T'_{op2}(z)$ and $T_{op2}(z)$ with grid impedance L_g.
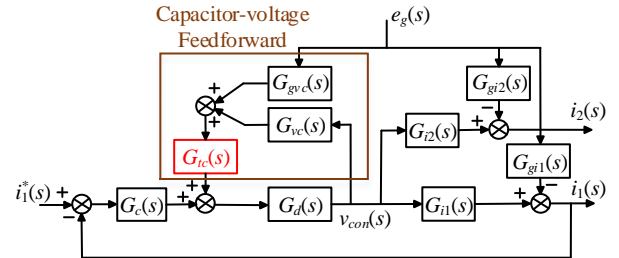

Fig. 26. Grid-side current diagram with converter-side current feedback control and proposed capacitor voltage feedforward method.

For comparison, the low-frequency output admittance without capacitor voltage feedforward or with unit capacitor voltage feedforward are also derived as (30).

When multiple HCs with large enough integral gain k_{ih} are paralleled with the fundamental PR as (1), (30) can be approximated as (31) at the compensated frequencies by HCs.

$$Y_{o1}(s)\big|_{s=j\omega_h} = Y_{o2}(s)\big|_{s=j\omega_h}$$

$$\approx \frac{1}{(L_1+L_T)s}[L_1C_f s^2 +1 - \frac{1}{(L_TC_f s^2 +1)}] \approx \frac{L_1C_f s}{L_1+L_T} \quad (31)$$

From (29) and (31), it can be seen the proposed method has the same harmonic rejection capability as the ones with HCs. Fig. 27 shows the magnitude-frequency curves of $Y_{oc}(s)$, $Y_{o1}(s)$ and $Y_{o2}(s)$, where only 5th and 7th HCs are employed for $Y_{o1}(s)$ and $Y_{o2}(s)$. Here, $k_p=4$, $L_g=0$ and $C_f=5$ µF. As seen, compared with $Y_{o1}(s)$, the magnitude of $Y_{o2}(s)$ has a great dip in the low-frequency range due to the capacitor voltage feedforward, but is the same with $Y_{o1}(s)$ at the compensated frequencies by HCs. While for $Y_{oc}(s)$, its magnitude has a further decrease, and is equal to $Y_{o1}(s)$ and $Y_{o1}(s)$ at the compensated frequencies by HCs as analyzed in (29) and (31). It means that the proposed method is equivalent to paralleling a cluster of HCs with the fundamental PR, and meanwhile, due to the smooth magnitude curve of $Y_{oc}(s)$ in the low-frequency range, the proposed method shows a strong robustness against the variation of harmonic frequencies. For $Y_{o1}(s)$ and $Y_{o2}(s)$ with HCs, a small variation of harmonic frequencies Δf will lead to much reduced harmonic rejection capability shown in Fig. 27. Moreover, since HCs are not required for the proposed method, the structure of current control is greatly simplified, and the control parameters can be flexibly designed without having an extremely high bandwidth.

In conclusion, the proposed capacitor-voltage feedforward with full delay compensation can greatly improve the weak grids adaptability of *LCL*-filtered grid-connected converters. When incorporated with converter-side current feedback, the overall system features a strong robustness against grid impedance variation and grid background harmonics, and the structure of current control and its design complexity can also be simplified.

Fig. 27. Magnitude-frequency curves of the output admittance $Y_{oc}(s)$, $Y_{o1}(s)$ and $Y_{o2}(s)$.

TABLE II
SYSTEM PARAMETERS FOR EXPERIMENTS

Description	Symbol	Value
Grid voltage	e_g/V	90 (RMS)
Dc voltage	u_{dc}/V	200
Fundamental frequency	f_1/Hz	50
Switching frequency	f_{sw}/kHz	10
Sampling frequency	f_s/kHz	10
Proportional gain	k_p	4
Compensation coefficient	m	0.7

VI. EXPERIMENTAL RESULTS

A single-phase experimental prototype has been constructed, as shown in Fig.2, to validate the effectiveness of the proposed method. A digital microcontroller is used to perform the control of experimental prototype, which consists of a floating point DSP (Texas Instruments TMS320F28335) as the main algorithm controller, and a Xilinx FPGA XC3S400 as the assistant controller for implementing PWM signals output, ADC control, and fault protection, etc. The key experimental parameters are shown in Table II.

By setting a flag variable in the DSP, the time t_d used for

$$Y_{oc}(s) = \frac{1}{L_1L_TC_f s^3 +(L_1+L_T)s}[L_1C_f s^2 +1 - \frac{G_d(s)G_c(s)+G_{tc}(s)G_d(s)L_1s}{L_1L_TC_f s^3 +(L_1+L_T)s+G_d(s)G_c(s)(L_TC_f s^2 +1)-G_{tc}(s)G_d(s)L_Ts}] \quad (28)$$

$$Y_{oc}(s) \approx \frac{1}{(L_1+L_T)s}[L_1C_f s^2 +1 - \frac{G_d(s)G_c(s)+L_1s}{G_d(s)G_c(s)(L_TC_f s^2 +1)+L_1s}] \approx \frac{L_1C_f s}{L_1+L_T} \quad (29)$$

$$\begin{cases} Y_{o1}(s) \approx \frac{1}{(L_1+L_T)s}[L_1C_f s^2 +1 - \frac{G_d(s)G_c(s)}{(L_1+L_T)s+G_d(s)G_c(s)(L_TC_f s^2 +1)}] \\ Y_{o2}(s) \approx \frac{1}{(L_1+L_T)s}[L_1C_f s^2 +1 - \frac{G_d(s)G_c(s)+G_d(s)L_1s}{(L_1+L_T)s+G_d(s)G_c(s)(L_TC_f s^2 +1)-G_d(s)L_Ts}] \end{cases} \quad (30)$$

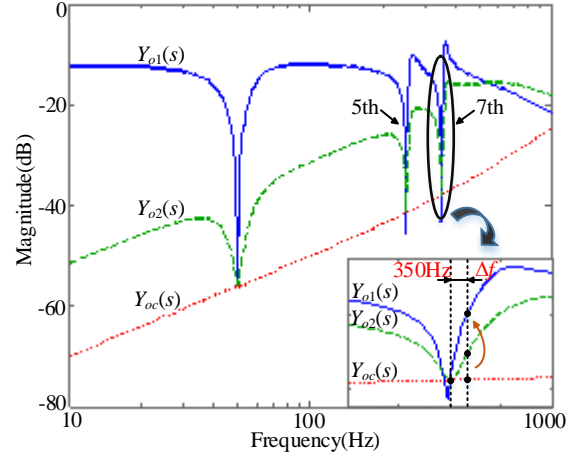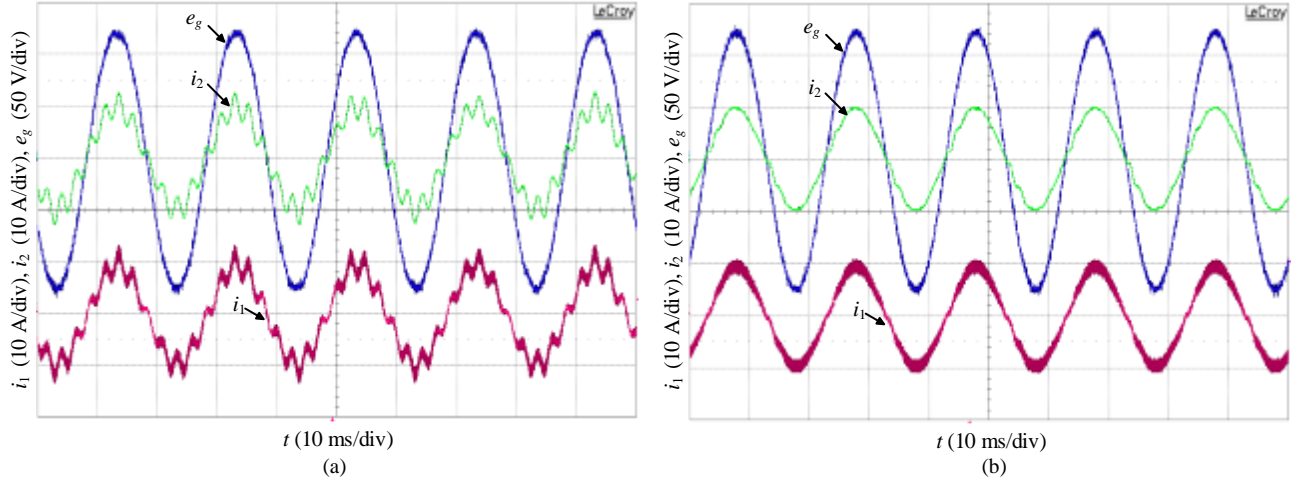Fig. 28. Steady-state experimental results with 5th and 7th HCs under L_g=2 mH. (a) Unit capacitor voltage feedforward. (b) Proposed method.
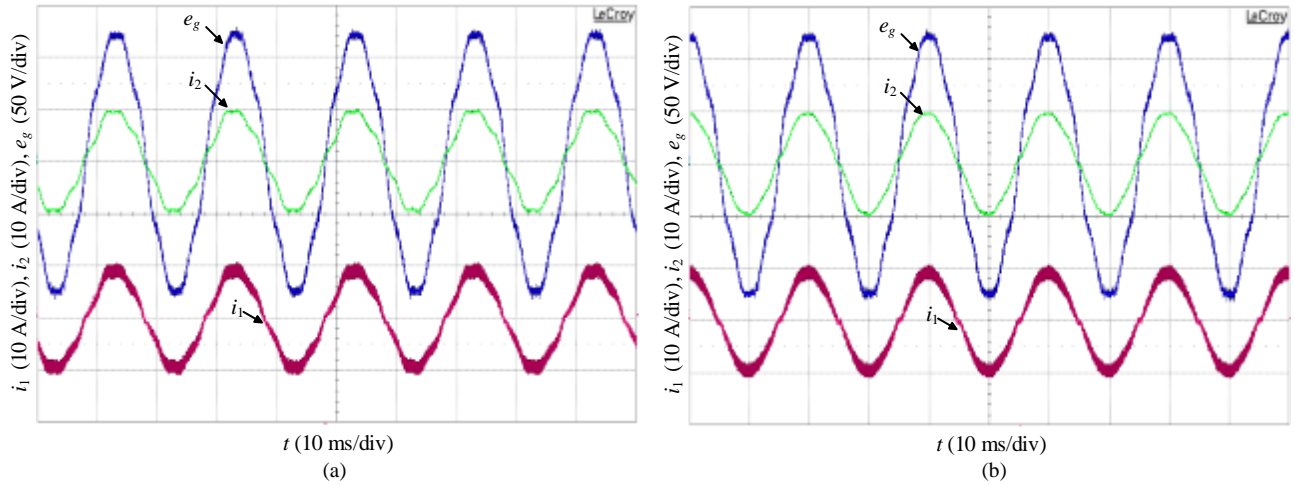

Fig. 29. Experimental results with 5th and 7th grid background harmonics. (a) Unit capacitor voltage feedforward. (b) Proposed method.

execution of capacitor voltage feedforward control is found to be 4.72 µs, which includes 4 µs sampling time t_{ad} of ADC and 0.72 µs calculation time t_{cd} for the half sampling period delay compensation link G'_{hc}. This delay time is much smaller than the sampling period T_s=100 µs, and its impact on the control system can be neglected. It should be noted that for high power applications where system switching frequency and sampling frequency are significantly reduced, e.g. $f_s = f_{sw} = 3$ kHz, the performance of the proposed control may be degraded due to the non-ideal half sampling period delay compensation $G'_{hc}(z)$. One possible solution is to adopt the multi-sampling technique proposed in [40].

The effect of grid impedance L_g on the low-frequency control bandwidth is investigated with HCs as discussed in Fig. 6. Here, unit capacitor voltage feedforward is also tested for comparison. From Section IV, the design constraints of *LCL*-filter, $\omega_r<\omega_s/3$ and (15), should be satisfied for unit capacitor voltage feedforward. C_f=10 µF is thus employed to ensure system stability. A 2mH inductor is in series with the grid-side inductor L_2 to simulate the grid impedance L_g, and in this scenario, (15) is still valid. Fig. 28

shows the steady-state experimental results with only 5th and 7th HCs under L_g=2mH. Since the system is always stable when L_g=0 with either unit capacitor voltage feedforward or the proposed method, the experimental results are not presented here. It can be seen from Fig. 28(a) the output current oscillates at about 7th~8th frequency. From Fig. 6(b), it is because the magnitude of the open-loop transfer function at f_2 (the frequency of -180° crossing caused by 7th HC) is less than or close to 0 dB due to grid impedance. While for the proposed method shown in Fig. 28(b), the output current is stable, because the low frequency characteristic of the system is independent of grid impedance as analyzed in Fig. 25.

Then the rejection capability of grid background harmonics is investigated. Here, 4% of 5th and 4% of 7th harmonics with respect to the fundamental component are injected by the programmable ac power supply. Fig. 29 shows the experimental results with unit capacitor voltage feedforward and the proposed method respectively, where HCs are not employed. It can be seen from Fig. 29(a) both the converter-side and grid-side current are seriously
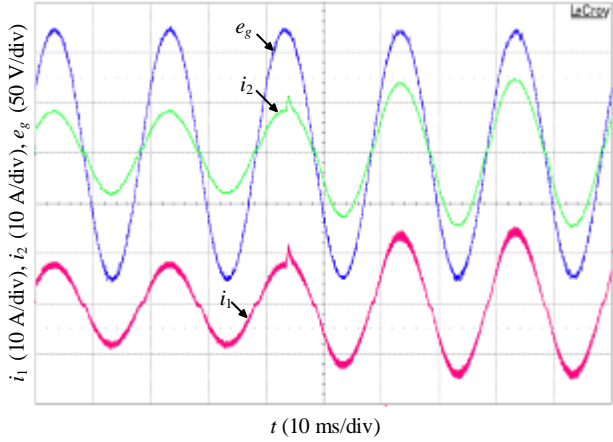
Fig. 30. Transient experimental results with the proposed method under ideal power grids.

distorted. While for the proposed method shown in Fig. 29(b), the converter-side current keeps a good sinusoidal waveform, and the slight distortion in the grid-side current is caused by the paralleled filter capacitor C_f branch.

From Section V *Part C*, no additional design constraints are required for the proposed method. To verify this, C_f=5 µF is selected, which will cause system instability for unit capacitor voltage feedforward. Fig. 30 shows the transient experimental results under ideal power grids. It can be seen the system is stable even though a step change of current reference is performed. The proposed method thus provides a more flexible design of *LCL*-filter without additional constraints.

Furthermore, 5th and 7th harmonics are also injected to test its control performance when C_f =5 µF. Fig. 31 shows the experimental results, where it is clear that even without using additional HCs, both the grid-side and converter-side currents are kept sinusoidal as those shown in Fig. 29(b). Comparing Fig. 31(a) with Fig. 31(b), the output current without HCs is almost the same as the one with HCs, which verifies the theoretical analysis in Section V *Part D*. Thus, the proposed method is equivalent to paralleling HCs with the fundamental PR, which greatly reduces the design complexity of current control. Fig. 31(c) shows the transient experimental results without HCs. As seen, the system still keeps good harmonic rejection capability during the transient.

VII. Conclusion

This paper has investigated the adaptability of *LCL*-filtered grid-connected converters with converter-side current feedback under weak grid operation, e.g., grid impedance variation and grid background harmonics. An improved capacitor voltage feedforward with full delay compensation has been proposed, which can keep the low-frequency characteristic of the system independent of grid impedance variation. It is also identified that the system has very low output admittance over a wide range of frequencies. Therefore, it is possible to achieve good grid background
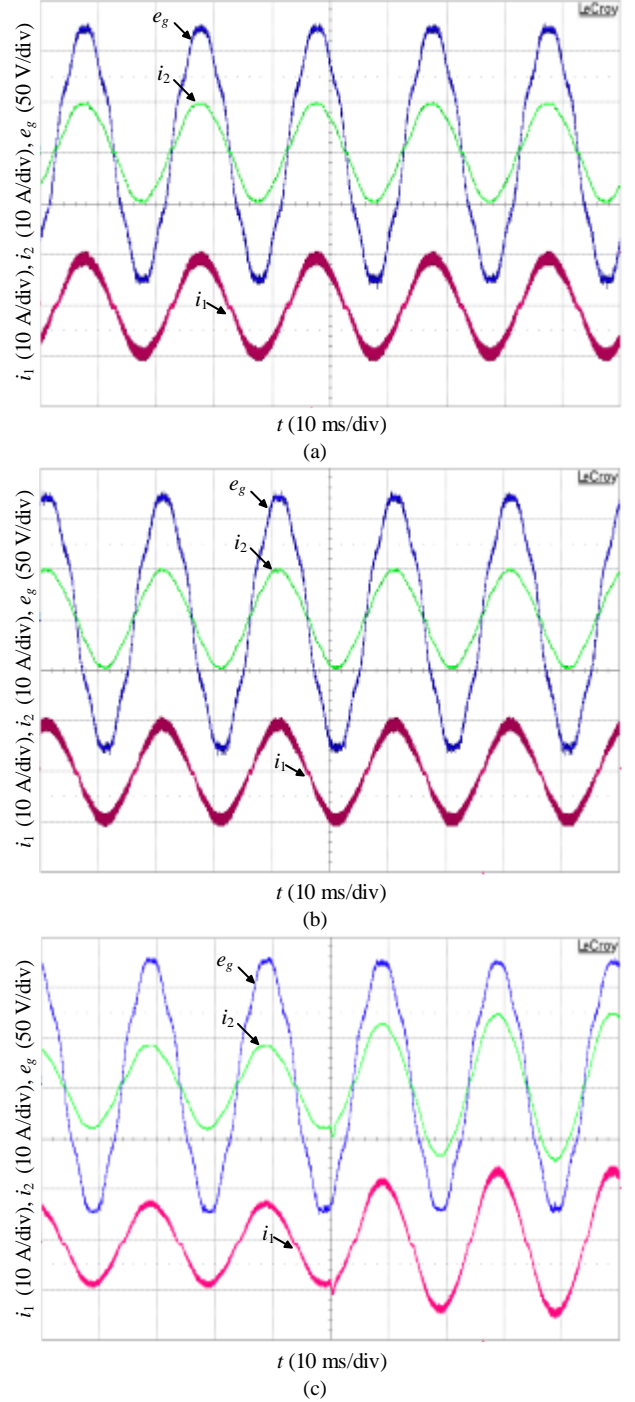
Fig. 31. Experimental results with the proposed method under 5th and 7th grid background harmonics. (a) Steady-state without 5th and 7th HCs. (b) Steady-state with 5th and 7th HCs. (c) Transient without 5th and 7th HCs.

harmonic rejection even with frequency variation. More importantly, the proposed control greatly simplifies the structure of current control and its design, and the multiple HCs used in parallel with the conventional current control can be eliminated. In addition, the resonance frequency of *LCL*-filter can be designed to be above 1/6 of system

sampling frequency, indicating a wider control bandwidth and lower current distortion caused by the paralleled filter capacitor branch. All of these show that the proposed control can greatly enhance the adaptability of *LCL*-filtered grid-connected converters under weak grids. Experimental results are finally presented to verify the proposed control.

REFERENCES

[1] F. Blaabjerg, R. Teodorescu, M. Liserre, and A. V. Timbus, "Overview of control and grid synchronization for distributed power generation systems," *IEEE Trans. Ind. Electron.*, vol. 53, no. 5, pp. 1398-1409, Oct. 2006.

[2] M. Liserre, Teodorescu, and F. Blaabjerg, "Stability of photovoltaic and wind turbine grid-connected inverters for a large set of grid impedance values," *IEEE Trans. Power Electron.*, vol. 21, no. 1, pp. 263-272, Jan. 2006.

[3] P. C. Loh, Y. Tang, F. Blaabjerg, and P. Wang, "Mixed-frame and stationary-frame repetitive control schemes for compensating typical load and grid harmonics," *IET Power Electron.*, vol. 4, no. 2, pp. 218-226, 2011.

[4] D. Yang, X. Ruan, and H. Wu, "Impedance shaping of the grid-connected inverter with *LCL* filter to improve its adaptability to the weak grid condition," *IEEE Trans. Power Electron.*, vol. 29, no. 11, pp. 5795-5805, Nov. 2014.

[5] X. Li, X. Wu, Y. Geng, X. Yuan, C. Xia, and X. Zhang, "Wide damping region for *LCL*-type grid-connected inverter with an improved capacitor-current-feedback method," *IEEE Trans. Power Electron.*, vol. 30, no. 9, pp. 5247-5259, Sep. 2015.

[6] D. Pan, X. Ruan, C. Bao, W. Li, and X. Wang, "Capacitor-current-feedback active damping with reduced computation delay for improving robustness of *LCL*-type grid-connected inverter," *IEEE Trans. Power Electron.*, vol. 29, no. 7, pp. 3414-3427, Jul. 2014.

[7] Z. Xin, P. C. Loh, X. Wang, F. Blaabjerg, and Y. Tang, "Highly accurate derivatives for *LCL*-filtered grid converter with capacitor voltage active damping," *IEEE Trans. Power Electron.*, vol. 31, no. 5, pp. 3612-3625, May 2016.

[8] Y. Tang, P. C. Loh, P. Wang, F. H. Choo, and F. Gao, "Exploring inherent damping characteristic of *LCL*-filters for three-phase grid-connected voltage source inverters," *IEEE Trans. Power Electron.*, vol. 27, no. 3, pp. 1433-1443, Mar. 2012.

[9] X. Wang, F. Blaabjerg, and P. C. Loh, "Grid-current-feedback active damping for *LCL* resonance in grid-connected voltage-source converters," *IEEE Trans. Power Electron.*, vol. 31, no. 1, pp. 213-223, Jan. 2016.

[10] J. Wang, J. Yan, and L. Jiang, "Pseudo-derivative-feedback current control for three-phase grid-connected inverters with *LCL* filters," *IEEE Trans. Power Electron.*, vol. 31, no. 5, pp. 3898-3912, May 2016.

[11] M. Hanif, V. Khadkikar, W. Xiao, and J. L. Kirtley, "Two degrees of freedom active damping technique for *LCL* filter-based grid connected PV systems," *IEEE Trans. Ind. Electron.*, vol. 61, no. 6, pp. 2795-2803, Jun. 2014.

[12] W. Yao, Y. Yang, X. Zhang, F. blaabjerg, and P. C. Loh, "Design and analysis of robust active damping for *LCL* filters using digital notch filters," *IEEE Trans. Power Electron.*, vol. 32, no. 3, pp. 2360-2375, Mar. 2017.

[13] J. Wang, J. Yan, L. Jiang, and J. Zou, "Delay-dependent stability of single-loop controlled grid-connected inverters with *LCL* filters," *IEEE Trans. Power Electron.*, vol. 31, no. 1, pp. 743-757, Jan. 2016.

[14] S. Zhou, X. Zou, D. Zhu, Y. Kang, L. Tong, and X. Gao, "*LCL* type grid-connected converter no startup inrush current control method based on capacitor branch voltage feedforward," in *Proc. IEEE IECON*, 2015, pp. 1471-1476.

[15] M. Zhao, X. Yuan, J. Hu, and Y. Yan, "Voltage dynamics of current control time-scale in a VSC-connected weak grid," *IEEE Trans. Power Syst.*, vol. 31, no. 4, pp. 2925-2937, Jul. 2016.

[16] J. Xu, Q. Qian, S. Xie, and B. Zhang, "Grid-voltage feedforward based control for grid-connected *LCL*-filtered inverter with high robustness and low grid current distortion in weak grid," in *Proc. IEEE APEC*, 2016, pp. 1919-1925.

[17] T. Abeyasekera, C. M. Johnson, D. J. Atkinson, and M. Armstrong, "Suppression of line voltage related distortion in current controlled grid connected inverters," *IEEE Trans. Power Electron.*, vol. 20, no. 6, pp. 1393-1401, Nov. 2005.

[18] X. Wang, X. Ruan, S. Liu, and C. K. Tse, "Full feedforward of grid voltage for grid-connected inverter with *LCL* filter to suppress current distortion due to grid voltage harmonics," *IEEE Trans. Power Electron.*, vol. 25, no. 12, pp. 3119-3127, Dec. 2010.

[19] Y. Liu, W. Wu, Y. He, Z. Lin, F. Blaabjerg, and H. S.-H. Chung, "An efficient and robust hybrid damper for *LCL*- or *LLCL*-based grid-tied inverter with strong grid-side harmonic voltage effect rejection," *IEEE Trans. Ind. Electron.*, vol. 63, no. 2, pp. 926-936, Feb. 2016.

[20] A. Timbus, M. Liserre, R. Teodorescu, P. Rodriguez, and F. Blaabjerg, "Evaluation of current controller for distributed power generation systems," *IEEE Trans. Power Electron.*, vol. 24, no. 3, pp. 654-664, Mar. 2009.

[21] Y. A. - R. I. Mohamed, "Suppression of low- and high-frequency instabilities and grid-induced disturbances in distributed generation inverters," *IEEE Trans. Power Electron.*, vol. 26, no. 12, pp. 3790-3803, Dec. 2011.

[22] J. Xu, S. Xie, and T. Tang, "Evaluations of current control in weak grid case for grid-connected *LCL*-filtered inverter," *IET Power Electron.*, vol. 6, no. 2, pp. 227-234, 2013.

[23] Y. He, K. Wang, and H. S. Chung, "Utilization of proportional filter capacitor voltage feedforward to realize active damping for digitally-controlled grid-tied inverter operating under wide impedance variation," in *Proc. IEEE ECCE*, 2014, pp. 4450-4457.

[24] C. Citro, P. Siano, and C. Cecati, "Designing inverters' current controllers with resonance frequencies cancellation," *IEEE Trans. Ind. Electron.*, vol. 63, no. 5, pp. 3072-3080, May 2016.

[25] C. Zou, B. Liu, S. Duan, and R. Li, "A feedforward scheme to improve system stability in grid-connected inverter with *LCL* filter," in *Proc. IEEE ECCE*, 2013, pp. 4476-4480.

[26] J. He, Y. Li, D. Bosnjak and B. Harris, "Investigation and active damping of multiple resonances in a parallel-inverter-based microgrid," *IEEE Trans. Power Electron.*, vol. 28, no. 1, pp. 234-246, Jan. 2013.

[27] J. He, Y. Li, R. Wang, and C. Zhang, "Analysis and mitigation of resonance propagation in grid-connected and islanding microgrids," *IEEE Trans. Energy Convers.*, vol. 30, no. 1, pp. 70-81, Mar. 2015.

[28] J. He, and Y. Li, "Generalized closed-loop control schemes with embedded virtual impedances for voltage source converters with *LC* or *LCL* filters," *IEEE Trans. Power Electron.*, vol. 27, no. 4, pp. 1850-1861, Apr. 2012.

[29] J. Dannehl, F. W. Fuchs, S. Hansen, and P. B. Thøgersen, "Investigation of active damping approaches for PI-based current control of grid-connected pulse width modulation converters with *LCL* filters," *IEEE Trans. Ind. Appl.*, vol. 46, no. 4, pp. 1509-1517, Jul./Aug. 2010.

[30] S. Golestan, M. Monfared, F. D. Freijedo, and J. M. Guerrero, "Dynamics assessment of advanced single-phase PLL structures," *IEEE Trans. Ind. Electron.*, vol. 60, no. 6, pp. 2167-2177, Jun. 2013.

[31] Y. Han, M. Luo, X. Zhao, J. M. Guerrero, and L. Xu, "Comparative performance evaluation of orthogonal-signal-generators-based single-phase PLL algorithms-a survey," *IEEE Trans. Power Electron.*, vol. 31, no. 5, pp. 3932-3944, May 2016.

[32] T. Nussbaumer, M. L. Heldwein, G. Gong, S. D. Round, and J. W. Kolar, "Comparison of prediction techniques to compensate time delays caused by digital control of a three-phase buck-type PWM rectifier system," *IEEE Trans. Ind. Electron.*, vol. 55, no. 2, pp. 791-799, Feb. 2008.

[33] Q. Yan, X. Wu, X. Yuan, and Y. Geng, "An improved grid-voltage feedforward strategy for high-power three-phase grid-connected inverter based on the simplified repetitive predictor," *IEEE Trans. Power Electron.*, vol. 31, no. 5, pp. 3880-3897, May 2016.

[34] P. Mattavelli, F. Polo, F. D. Lago, and S. Saggini, "Analysis of control-delay reduction for the improvement of UPS voltage-loop bandwidth," *IEEE Trans. Ind. Electron.*, vol. 55, no. 8, pp. 2903-2911, Aug. 2008.

[35] H. Deng, R. Oruganti, and D. Srinivasan, "PWM methods to handle time delay in digital control of a UPS Inverter," *IEEE Power Electron. Letters*, vol. 3, no. 1, pp. 1-6, Mar. 2005.

[36] D. Yang, X. Ruan and H. Wu, "A real-time computation method with dual sampling mode to improve the current control performance of the *LCL*-type grid-connected inverter," *IEEE Trans. Ind. Electron.*, vol. 62, no. 7, pp. 4563-4572, Jul. 2015.

[37] C. Chen, J. Xiong, Z. Wan, J. Lei, and K. Zhang, "A time delay compensation method based on area equivalence for active damping of an *LCL*-type converter," *IEEE Trans. Power Electron.*, vol. 32, no. 1, pp. 762-772, Jan. 2017.

[38] K. Zhou, and D. Wang, "Digital repetitive controlled three-phase PWM rectifier," *IEEE Trans. Power Electron.*, vol. 18, no. 1, pp. 309-316, Jan. 2003.

[39] K. Zhang, Y. Kang, J. Xiong, and J. Chen, "Direct repetitive control of SPWM inverter for UPS purpose," *IEEE Trans. Power Electron.*, vol. 18, no. 3, pp. 784-792, May 2003.

[40] X. Zhang, P. Chen, C. Yu, F. Li, H. Do and R. Cao, "Study of current control strategy based on multi-sampling for high-power grid-connected inverters with *LCL*-filter," *IEEE Trans. Power Electron.*, 2016. (Published online)

Xiaoqiang Li (M'16) received the B.S. and Ph.D. degrees from the School of Information and Electrical Engineering, China University of Mining and Technology, Xuzhou, China, in 2010 and 2015, respectively. He is currently a Research Fellow with Nanyang Technological University, Singapore. His current research interests include renewable energy generation and digital control in power electronics.

Jingyang Fang (S'15) received the B.Sc. degree and the M.Sc. degree in electrical engineering from Xi'an Jiaotong University, Xi'an, China, in 2013 and 2015, respectively. He is currently working toward the Ph.D. degree in Nanyang Technological University, Singapore.
His research interests include power quality control, renewable energy generation and digital control in power electronics.

Yi Tang (S'10-M'14) received the B.Eng. degree in electrical engineering from Wuhan University, Wuhan, China, in 2007 and the M.Sc. and Ph.D. degrees from the School of Electrical and Electronic Engineering, Nanyang Technological University, Singapore, in 2008 and 2011, respectively.
From 2011 to 2013, he was a Senior Application Engineer with Infineon Technologies Asia Pacific, Singapore. From 2013 to 2015, he was a Postdoctoral Research Fellow with Aalborg University, Aalborg, Denmark. Since March 2015, he has been with Nanyang Technological University, Singapore as an Assistant Professor. He is the Cluster Director in advanced power electronics research program at the Energy Research Institute @ NTU (ERI@N).
Dr. Tang serves as an Associate Editor for the IEEE JOURNAL OF EMERGING AND SELECTED TOPICS IN POWER ELECTRONICS. He received the Infineon Top Inventor Award in 2012.

Xiaojie Wu (M' 15) received the B.S. degree in industrial automation and the M.S. and Ph.D. degrees in electrical engineering from China University of Mining and Technology, Xuzhou, China, in 1988, 1991, and 2000, respectively.
From 2002 to 2004, he was a Postdoctoral Research Fellow with Tsinghua University, Beijing, China. Since 1991, he has been with the School of Information and Electrical Engineering, China University of Mining and Technology, where he is currently a Professor. He has authored or coauthored one book and more than 60 technical papers published in journals and conferences. His research interests include renewable energy generation systems, multilevel converters, advanced control of electrical machines, and power electronics.

Yiwen Geng received the B.S., M.S., and Ph.D. degrees from the School of Information and Electrical Engineering, China University of Mining and Technology, Xuzhou, China, in 2000, 2004, and 2014, respectively. Since 2006, he has been with the School of Information and Electrical Engineering, China University of Mining and Technology, where he is currently an Associate Professor. His current research interests include active power filter and renewable energy generation systems.